Comparison of Future Aviation Fuels to Minimize the Climate Impact of Commercial Aircraft

Proesmans, P.; Vos, Roelof

DOI
10.2514/6.2022-3288

Publication date
2022

Document Version
Final published version

Published in
AIAA AVIATION 2022 Forum

Comparison of Future Aviation Fuels to Minimize the Climate Impact of Commercial Aircraft

P. Proesmans* and R. Vos†
Delft University of Technology, Kluyverweg 1 2629HS, Delft, The Netherlands

Sustainable aviation fuel (SAF) and liquid hydrogen are currently being studied to replace kerosene in commercial aviation to reduce global warming. In this study, the question is how do the airplane design variables change when minimizing the global warming impact of aircraft powered by SAF or LH2? Secondly, how do these aircraft compare in terms of climate impact and operating costs, considering regional, medium-, and long-range categories? A multidisciplinary design optimization process varies airframe, turbofan engine and mission design variables to obtain the cost- and climate-optimal design solutions. A linearized temperature response model evaluates the average temperature response over 100 years considering both CO_2 and non-CO_2 effects. The trade-off between climate impact reduction on the one hand and operating cost, on the other hand, is studied for each fuel type and aircraft category. We conclude that LH2 can achieve the largest reduction in temperature response in all categories. The maximum reduction of 98% compared to the cost-optimal kerosene aircraft comes at an estimated increase of 30, 42, or 69% in operating costs for regional, medium-, and long-range missions. The SAF aircraft can reduce the climate impact by 86, 82, and 72% for regional, medium-range, and long-range aircraft. These savings lead to an 8, 14, and 26% increase in operating costs. The analysis shows that the SAF-powered aircraft are preferred over the cost-optimal hydrogen aircraft for the regional and medium-range categories. Hydrogen does provide a Pareto-optimal solution for long-range aircraft, albeit at a significant in-flight energy and cost penalty.

Nomenclature

Latin Symbols

A	aspect ratio [-]
b	wing span [m]
C_L	lift coefficient [-]
C_D	drag coefficient [-]
C_{D_0}	zero-lift drag coefficient [-]
d	diameter [m]
E	in-flight energy consumption [MJ]
EI_i	emission index of species i [kg/kg]
e	Oswald factor [-]
F	objective function
$\mathbf{g}$	constraint vector
h	altitude [m or ft]
$(h/r)_{\mathrm{dome}}$	tank dome height-to-radius ratio [-]
l	length [m]
m	mass [kg]
M	Mach number [-]
r	range [km]
S	wing area [m^2]
T	thrust [kN] or temperature [K]
t	time [hours or years]
$\mathrm{U}_{\mathrm{ann}}$	annual utilization [hours/year]
v	velocity [m/s]
V	volume [m^3]
W	weight [kN]
$\mathbf{x}$	design vector

Greek Symbols

ΔT	surface temperature change [K]
η_{grav}	gravimetric index [-]
η_{ov}	overall propulsion efficiency [-]
$\Lambda_{0.25}$	wing quarter-chord sweep angle [deg]
λ	wing taper ratio [-]
Π	pressure ratio [-]

Sub- and Superscripts

0	sea-level condition or initial value
afse	airframe systems and equipment
app	approach condition
bl	block mission parameter

*PhD Candidate, Faculty of Aerospace Engineering, P.Proesmans@tudelft.nl, AIAA Student Member
†Assistant Professor, Faculty of Aerospace Engineering, R.Vos@tudelft.nl, AIAA Associate Fellow

core	core flow
cr	cruise condition
fus	fuselage
L	lower bound
ops	operations
eng	engine
TO	take-off condition
U	upper bound
$*$	optimal solution

Acronyms

ATR	average temperature response
BPR	bypass ratio
COC	cash operating cost
HPC	high pressure compressor
HT	horizontal tail
LHV	lower heating value of fuel [J/kg]
LPC	low pressure compressor
MAC	mean aerodynamic chord
MTOM	maximum take-off mass [kg]
OEM	operating empty mass [kg]
OPR	overall pressure ratio
RF	radiative forcing [W/m^2]
RPK	revenue passenger kilometer
SEC	specific energy consumption [$MJ/(N\,s)$]
TET	turbine entry temperature [K]
TLAR	top-level airplane requirement
TSFC	thrust specific fuel consumption [$kg/(N\,s)$]
VT	vertical tail
XDSM	extended design structure matrix

I. Introduction

Achieving climate-neutral aviation may require more than a single new technology or policy. To reach the goals set for carbon dioxide (CO_2) emissions, experts advocate a combination of improved operations, new technologies and new fuels [1, 2]. Although the efficiency of kerosene-powered aircraft continues to increase, annual improvements of 1 to 2% are unlikely to suffice when the objective is to achieve net-zero carbon emissions by 2050. Alternatively, novel fuels, such as liquid hydrogen (LH2) and sustainable aviation fuel (SAF) can provide more sustainable solutions. These fuel types can offer significant savings in terms of CO_2 but also affect the aircraft design, costs and non-CO_2 climate effects, such as the formation of condensation trails ("contrails") and NO_x emissions.

Sustainable aviation fuels contain hydrocarbon molecules and have properties similar to those of regular kerosene. These fuels can be produced through several pathways such as from feedstock or a combination of captured CO_2 and hydrogen (H_2) [3, 4]. Since each of these sources, indirectly or directly, take up CO_2 from the atmosphere, the life-cycle greenhouse gases (GHG) reduce by approximately 70 to 99% by using SAF compared to fossil Jet-A fuel [3, 4]. Furthermore, the reduction of soot emissions of SAF decreases the ice particle number in the exhaust gas and alters the contrail properties [5, 6]. Additionally, the airframe and engines do not require major changes to accommodate these fuels. Nevertheless, estimates have shown that these fuels will be more expensive than fossil-based kerosene [4] as well as electrically-produced liquid hydrogen [2].

On the other hand, non-hydrocarbon fuels provide a solution to eliminating the climate effects of CO_2. A promising alternative in this category is liquid hydrogen [7]. Compared to kerosene, hydrogen combustion emits more water vapor that acts both as a greenhouse gas and causes more frequent contrail formation. Nevertheless, experts have estimated that the radiative forcing of the contrails is lower compared to current contrails [6, 8, 9] and that the NO_x emissions can be reduced due to the wider flammability limits and the shorter burn time of hydrogen [2, 10, 11]. Additionally, hydrogen has a calorific value that is approximately 2.8 times higher than that of kerosene, reducing the fuel mass. On the other hand, liquid hydrogen has to be stored cryogenically and requires a larger volume per unit of energy. These properties complicate the integration into aircraft [12–14].

Researchers have assessed SAF and hydrogen separately [3, 14]. These studies imposed different aircraft requirements and used methods of varying fidelity. As a result, a consistent comparison between the applications of such novel fuels across different aircraft categories is missing.

This paper compares these future aviation fuels for fixed sets of aircraft requirements with equal fidelity. We consider three aircraft categories: regional, medium-range and long-range aircraft. This analysis yields insights into what fuel provides the best solution for each category when we wish to minimize the climate impact of aviation. For each category, we identify the climate impact reduction potential of hydrogen- and SAF-powered aircraft compared to a cost-optimal, kerosene-fueled design. Moreover, we monitor how climate-optimal designs influence operating costs and energy consumption.

We use multidisciplinary design optimization (MDO) with empirical and physics-based methods to design and optimize the aircraft. For each category, the same algorithm is used to optimize the aircraft for three different objectives: minimizing climate impact, minimizing operating costs and minimizing energy usage. The chosen climate-impact

metric is the average temperature response over 100 years (ATR100) and considers both CO_2 and non-CO_2 effects. This multi-objective approach allows us to study the trade-off between conflicting design objectives and can help to determine which fuel to allocate to which aircraft category in future fleets.

The remainder of this paper is structured as follows. First, the optimization problem is formulated and the design and analysis methods are described in Section II. This method builds on previous work by the authors and is expanded in several directions. Subsequently, we verify and validate these expansions in the methodology in Section III. Section IV presents the results obtained from the optimization studies and compares the climate impact, costs and energy consumption of the three different fuels (kerosene, SAF, LH2) for each aircraft category. Finally, Section V summarizes the findings for each aircraft category and fuel type and proposes further research steps.

II. Optimization Setup and Methods

We use a multidisciplinary framework to design aircraft for different fuel types and analyze them at the same level of fidelity. A multidisciplinary design optimization (MDO) is performed for each aircraft category, for each fuel type, and for the three objectives. This section defines the MDO setup and describes the design and analysis modules.

A. Optimization Problem Definition

The MDO considers two main design objectives: minimizing the climate impact (ATR_{100}) or minimizing the cash operating costs (COC) of the aircraft. By first performing these minimization studies separately and later in a multi-objective manner, the trade-off between these two objectives can be studied within each aircraft category. Additionally, the optimal aircraft design and/or operational parameters can vary with the selected fuel. The general optimization problem for each combination of fuel and aircraft category can be formulated as follows (adapted from Reference [15]):

$$
\begin{aligned}
\underset{\mathbf{x}}{\text{minimize}} \quad & F(\mathbf{x}) = \mathrm{ATR}_{100}(\mathbf{x}) \quad \text{or} \quad \mathrm{COC}(\mathbf{x}) \\
\text{subject to} \quad & W/S \leq \frac{1}{2}\rho_0 \left(\frac{v_{\mathrm{app}}}{1.23}\right)^2 C_{L_{\max}} f_{\mathrm{W}}, \\
& b \leq b_{\max}, \\
& \mathrm{TET}_{\mathrm{TO}} \leq \mathrm{TET}_{\mathrm{TO,\,max}}, \\
& \mathrm{OPR}_{\mathrm{cr}} \leq \mathrm{OPR}_{\mathrm{cr,\,max}}, \\
& C_{L_{\mathrm{cr}}} \leq \frac{C_{L_{\mathrm{buffet}}}}{1.3} = \frac{0.86 \cdot \cos \Lambda_{0.25}}{1.3}, \\
& x_i^L \leq x_i \leq x_i^U \qquad \text{for } i = 1, 2, ..., 9
\end{aligned}
\tag{1}
$$

In the above equation, $\mathbf{x}$ is the design vector consisting of nine design variables related to the airframe, engines and mission. Table 1 summarizes these variables and their bounds. Furthermore, the four constraints in Equation (1) confine the design space [16]. Firstly, the approach speed v_{app} limits the wing loading W/S at landing. The factor f_W translates the required wing loading at maximum landing mass (MLM) to a constraint on the wing loading at maximum take-off mass (MTOM). The second constraint ensures the wing span b remains smaller than the maximum span set by the aerodrome reference code. The approach speed v_{app} , factor f_W and maximum span $b_{\max}$ are included in the requirements specification in Section II.C.

The third constraint applies to the turbine entry temperature at take-off ($\mathrm{TET_{TO}}$), which should not rise above 2000 K, considering current cooling and material limitations. We limit the maximum overall pressure ratio to 60 according to current state-of-the-art technology. Finally, a ceiling on the cruise lift coefficient ($C_{L_{\mathrm{cr}}}$) is set such that a maneuver with a load factor of 1.3 can be completed without exceeding the aircraft lift coefficient at which buffeting occurs ($C_{L_{\mathrm{buffet}}}$).

Figure 1 presents the overall structure of the multidisciplinary design optimization. An optimization algorithm feeds the design vector to the aircraft design iterations. This design convergence ensures that each aircraft is consistent in terms of mass, geometry, and mission performance. Steps 6 and 7 in Figure 1 evaluate the climate impact and costs of a particular aircraft. These analyses provide the objective function values to the optimizer module. The latter then provides an update of the design vector, taking into account the constraint violations determined in step 8.

Table 1 Aircraft design variables and their respective bounds [15]

Variable	Description [Unit]	Lower Bound ($\mathbf{x}^L$)	Upper Bound ($\mathbf{x}^U$)
W/S	Wing loading [kN/m^2]	4.00	8.30
A	Aspect ratio [-]	5.00	12.0
BPR	Bypass ratio [-]	6.00	11.0
Π_{fan}	Fan pressure ratio [-]	1.20	1.80
Π_{lpc}	LPC pressure ratio [-]	1.20	1.80
Π_{hpc}	HPC pressure ratio [-]	15.0	25.0
TET	Turbine entry temperature [K]	1300	1700
h_{cr}	Initial cruise altitude [km]	6.00	12.0
M_{cr}	Cruise Mach number [-]	0.60	0.90

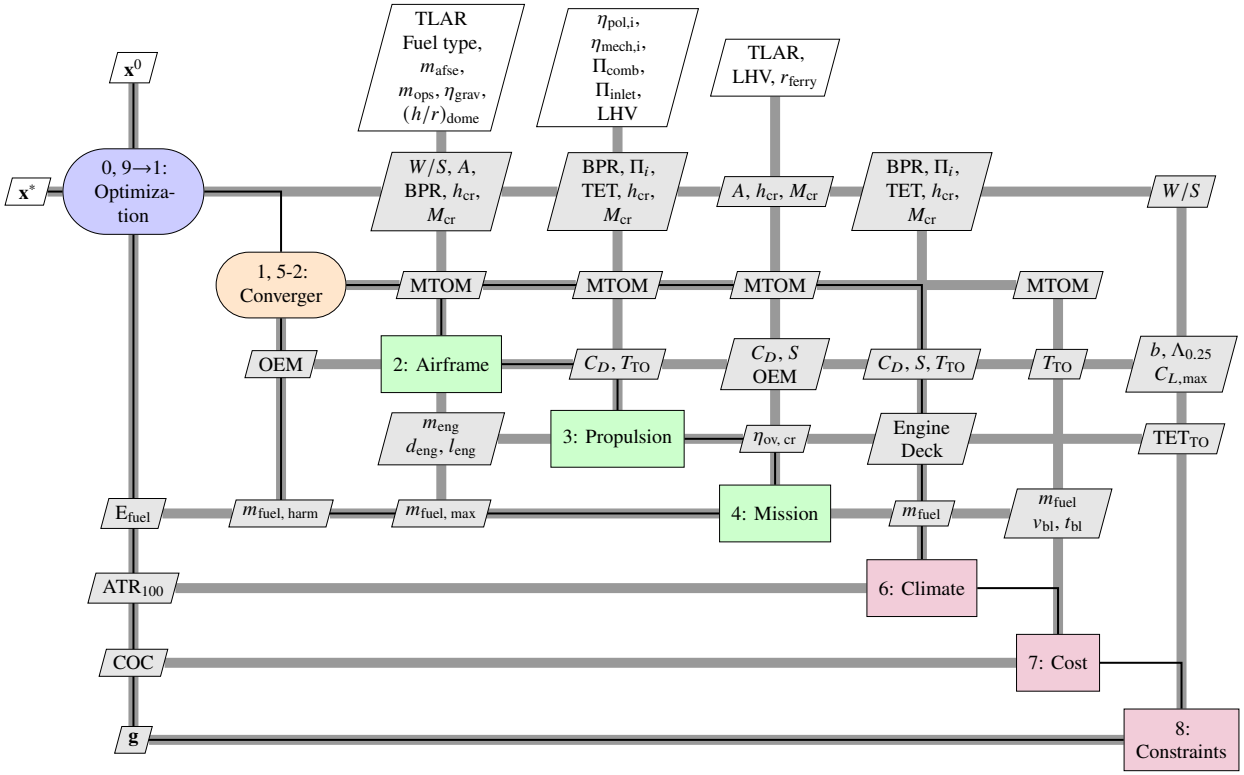

Fig. 1 Extended design structure matrix of multidisciplinary design optimization setup [15].

B. Design and Analysis Methods

The overall methodology consists of three main design disciplines, indicated by the green blocks in Figure 1. Although the design strategy is independent of the fuel type, the steps and assumptions in the disciplines change with the selected fuel and aircraft category. Therefore, this section describes these design steps in more detail. Since the methods for medium-range, kerosene and hydrogen aircraft have been introduced in previous research [15, 16], the focus in this section is the method extension stemming from the analysis of SAF as well as the application to the three different categories.

1. Airframe

The airframe design step, block 2 in Figure 1, consists of four smaller disciplines, namely the Class-I sizing process, the geometry creation, the conceptual aerodynamic analysis and the Class-II mass estimation. These modules determine the mass, geometry, and aerodynamic characteristics of the wing, fuselage and empennage. The following paragraphs elaborate further on these four design steps.

Class-I Sizing This step provides an estimate of the wing surface area S and the total take-off thrust, T_{TO}. These two parameters are determined from the wing loading W/S, a design variable, and the minimum thrust-to-weight ratio (T/W) which satisfies performance constraints related to the take-off distance, cruise speed and altitude, and climb gradients according to CS25 regulations. The program automatically selects the minimum T/W value which satisfies these requirements for the selected wing loading [16].

Geometry Creation A conceptual geometry of the aircraft is generated in each iteration, based on the well-known tube-and-wing configuration. This geometry prediction is used in the aerodynamic and structural disciplines to estimate the operating empty mass (OEM) and drag polar. During the optimization, mainly the wing and empennage planforms change as a result of the aspect ratio, wing loading and Mach number. The fuselage geometry is independent of the design vector for the kerosene- and SAF-powered aircraft, while the fuselage length of the hydrogen aircraft varies with the amount of hydrogen on board.

The fuselage is mainly sized around the passenger cabin and cargo compartment, which are modeled after the three reference aircraft being the Embraer 175, Airbus A320 and Airbus A350. The assumed cabin length, unit load devices, and resulting fuselage diameters are provided in Table 2. A four-meter-long cockpit is added in front of this cabin and a tail extension* is added to the rear. The length of this tail extension is computed using the statistical fineness ratios $(l/d)_{\mathrm{tail}}$ in Table 2, where d is the outer fuselage diameter.

Table 2 Geometric assumptions for varying aircraft categories

Parameter [Unit]	Regional	Medium-Range	Long-Range
Cabin length l_{cabin} [m]	21.3	27.0	51.8
Unit load devices	None	LD3-45	$2 \times$ LD3
Fuselage inner diameter $d_{\mathrm{fus,\ inner}}$ [m]	2.83	3.91	5.65
Fuselage outer diameter $d_{\mathrm{fus,\ outer}}$ [m]	2.98	4.06	5.99
Horizontal tail volume coefficient V_{HT} [-]	1.4	1.1	0.7
Horizontal tail aspect ratio A_{HT} [-]	4.5	5.0	4.4
Vertical tail volume coefficient V_{VT} [-]	0.13	0.085	0.051
Vertical tail aspect ratio A_{VT} [-]	1.8	1.7	1.7
Tail section fineness ratio $(l/d)_{\mathrm{tail}}$ [-]	2.1	1.6	1.6

For the hydrogen aircraft, a cylindrical tank with spherical endcaps is added behind the cabin in the rear-fuselage section. The tank is sized according to the maximum fuel it has to hold, according to the conceptual methods introduced in Reference [15]. The fuselage tank causes the longitudinal center-of-gravity (c.g.) to shift rearwards and also leads to a larger c.g. excursion, compared to the kerosene and SAF counterparts. These two aspects are reflected in the position of the main wing and the size of the empennage.

The wing planform construction is similar for all aircraft types. The aspect ratio and surface area, from the Class-I sizing, determine the wing span. The cruise Mach number dictates the quarter-chord sweep angle according to statistical data from Torenbeek [17] and Raymer [18]. This sweep angle subsequently drives the taper ratio, with higher sweep angles resulting in lower taper ratios to offload the tip sections. Furthermore, it is assumed that the trailing-edge sweep angle is zero up to 30% of the semi-span. This approach fully defines the 2D wing planform. Parameters such as dihedral and twist are neglected in this conceptual sizing method.

*The tail extension is defined as the distance from the aft-pressure bulkhead to the tip of the fuselage. The tail cone is typically longer than this, housing a part of the cabin.

The horizontal and vertical tail surface areas result from statistical volume coefficients, which are kept constant throughout the optimizations. These volume coefficients together with the tail surface aspect ratios are summarized in Table 2. The quarter-chord sweep angle of the horizontal and vertical tails are assumed to be 3 and 10 degrees more than the quarter-chord sweep angle of the main wing, respectively.

Aerodynamic Analysis The aerodynamic performance of the aircraft is modeled as a quadratic drag polar [16]:

$$C_D = C_{D_0} + \beta \cdot C_L^2 \tag{2}$$

where the zero-lift drag component C_{D_0} is estimated from the geometry by adding the minimum profile drag contributions of all airplane components. This term also includes corrections for the drag caused by surface perturbations, such as doors, control-surface gaps, and antennas. The β factor in Equation (2) is equal to the inverse of the multiplication of the effective aspect ratio, estimated Oswald efficiency factor e and π. The Oswald efficiency factor varies with the aspect ratio according to the statistical relation discussed in Reference [16].

To correct the drag polar for take-off and landing configurations, constant contributions are added to C_{D_0} and e [16]. The maximum lift coefficient $C_{L,\max}$ also depends on the flap configuration. The lift coefficient in landing is considered the maximum which can be achieved and depends on the quarter-chord sweep angle of the wing [15]. The lift coefficient in take-off and clean configuration are assumed to be 0.3 and 0.6 lower, respectively, than $C_{L,\max}$ in the landing setting.

Class-II Mass Estimation The OEM of the aircraft is determined by employing the semi-empirical and statistical methods introduced by Torenbeek [17]. The initial geometry, mass estimate, engine thrust, and load conditions are inputs to these methods. The fuselage mass is largely driven by the outer shell area and the cabin floor mass, among other, smaller components. This makes the fuselage mass sensitive to the integration of hydrogen tanks aft of the cabin since this integration elongates the tail extension. This is reflected in the gross shell weight, while the cabin floor mass is constant for a particular aircraft category.

The structural mass of the wing depends on the geometry (surface area, sweep angle, taper ratio and span), loading conditions (ultimate load factor and dive speed), $C_{L,\max}$, and the design mass. Torenbeek specifies the design mass as the maximum aircraft all-up mass without fuel in the wing. Therefore, the maximum zero-fuel mass is used in the case of kerosene-powered or SAF-powered aircraft, while the maximum take-off mass is selected for the hydrogen aircraft, as the hydrogen tank is assumed to reside in the fuselage. Furthermore, correction factors are applied to consider the load alleviation due to two wing-mounted engines. The empennage mass is derived from statistical data, based on the horizontal and vertical tail surface areas and sweep angles.

Within each aircraft category, mass estimates of the operational items and airframe equipment are kept constant throughout the iterations since it is assumed that these contributions do not vary with the selected fuel type. For the hydrogen aircraft, the tank mass is approximated by assuming a fixed gravitational index η_{grav} of 0.4 which relates the tank mass to the maximum hydrogen mass it can hold, according to the following equation:

$$\eta_{\text{grav}} = \frac{m_{\text{tank}}}{m_{\text{tank}} + m_{\text{fuel}}} \Rightarrow m_{\text{tank}} = \frac{\eta_{\text{grav}} \cdot m_{\text{fuel}}}{1 - \eta_{\text{grav}}} \tag{3}$$

2. Propulsion and Fuel Properties

The aircraft in this study each feature two turbofan engines with a two-spool, separate-exhaust architecture. A one-dimensional thermodynamic sizing process is applied using the methods from Mattingly et al. [19]. These methods allow measuring the impact of engine design choices on fuel consumption and emissions, and in particular, provide the data required to use P3-T3 methods to estimate the NO_x emission index in off-design conditions. Previous research [16] discusses the verification and validation of these physics-based methods.

Various types of sustainable aviation fuels exist [4], including hydroprocessed esters and fatty acids (HEFA), alcohol-to-jet, and power-to-liquid SAF. In this study, we refer to the latter type as synthetic kerosene. In the optimizations presented in Section IV, we assume a 50-50 mixture of HEFA and kerosene as the sustainable aviation fuel. In the price sensitivity analysis in Section IV.D, also the effect of synthetic kerosene and a 100% SAF mixture is studied.

To account for the different fuel types in the thermodynamic on- and off-design analyses, the lower heating values (LHV) and the variable specific gas models are adapted. Additionally, the emission indices of the various species differ. Table 3 presents the LHV values and emissions indices used for the different fuels. SAF and hydrogen can e produced free of sulfur [3, 11] and hence the sulfate emissions are assumed to be zero. The sulfate emissions are scaled by the

mass percentage of fossil kerosene in the mixture. This assumption is a simplification, but the influence is assumed to be small because the climate impact due to soot aerosols is small compared to other contributions.

Table 3 Overview of calorific values and emission indices for fuel types under consideration [15, 20]

	Kerosene	**SAF 50%**	**SAF 100%**	**Hydrogen**
LHV [MJ/kg]	43.0	43.6	44.2	120
EI CO_2 [kg_{CO_2}/kg_{fuel}]	3.16	1.58	0.	0.
EI H_2O [kg_{H_2O}/kg_{fuel}]	1.26	1.32	1.36	8.93
EI Soot [kg_{Soot}/kg_{fuel}]	4.0×10^{-5}	2.0×10^{-5}	0.	0.
EI SO_4 [kg_{SO_4}/kg_{fuel}]	2.0×10^{-4}	1.0×10^{-4}	0.	0.

As can be seen from Table 3, the LHV of SAF fuel is slightly higher than that of fossil-based kerosene due to the lower aromatics content, which increases the number of carbon-hydrogen bonds and as a result, the energy content per unit of mass [21]. Due to the lack or reduction in aromatics, sustainable aviation fuels also have a higher hydrogen mass content. This explains why the water emission index is slightly larger in Table 3. The higher water emission index also influences the contrail formation criterion, as discussed in Section II.B.4.

The thermodynamic model of the engine cycle uses a variable specific heat model such that the isobaric specific heat c_p varies with temperature and fuel-to-air ratio. Since the SAF variants have a higher water content than kerosene, the gas in the turbines is characterized by a higher c_p value. Nevertheless, previous research [22] has shown that the influence of this difference on engine performance is negligible. Therefore, the same gas model from Walsh and Fletcher [23] is used both for kerosene and SAF-based propulsion. For the hydrogen-powered turbofan, the gas model is adapted to reflect the increase in water and lack of carbon molecules in the turbines [15].

3. Mission Performance

The mission analysis step in Figure 1 provides an update of the required fuel mass in the aircraft design loop, which, together with the updated OEM and specified payload mass, provides an update of the MTOM in the converger (process 1 in Figure 1). Additionally, for the hydrogen aircraft, the maximum required fuel is computed in this mission analysis step as a function of the engine and aerodynamic performance. The hydrogen mass is required to estimate the tank size and mass, and by consequence, to update the size of the fuselage, wing and empennage.

The fuel mass is updated using the conceptual lost-range method [24] to limit the computational cost in the design convergence process. For hydrogen aircraft, the statistical relations used to determine the reserve fuel are replaced by relations based on the Breguet range equations. This is done because the statistical terms do not correctly reflect the hydrogen consumption in the diversion and loiter phases. The required diversion range and loiter time for each aircraft category are included in Table 4.

4. Climate Impact

The climate impact is one of the optimization objectives in this study. The aim is to consider both CO_2 and non-CO_2 climate agents and to include both their short- and long-term effects. Therefore, the climate impact metric of choice is the average temperature response over 100 years (ATR_{100}). This parameter is defined as follows:

$$\mathrm{ATR}_{100} = \frac{1}{100} \int_0^{100} \Delta T(t)\, dt \tag{4}$$

Here, the expected temperature response ΔT, as a result of emissions and contrail formation, is integrated over a period of 100 years (the unit of t is years in Equation (4)) to provide a balanced assessment of long-term (CO_2 formation, methane and ozone depletion) and short-term radiative effects (ozone creation, contrails and water vapor at low altitudes). This period starts in the year that the aircraft model under consideration is introduced into the market. The hypothetical scenario is defined in Section II.C.

We determine temperature response ΔT in each year t with a linearized temperature response model. The working principle of this model and the assumptions for the case of kerosene have been laid out in previous research [15, 16, 25].

This section summarizes the particular model assumptions for each fuel type considered in this study. Since certain climate effects are still not fully understood, uncertainties are present in this climate model.

Kerosene The climate impact of kerosene is caused by the emissions of CO_2, NO_x, soot, SO_4 and the formation of contrails and consequently contrail-induced cirrus. While CO_2 is a greenhouse gas itself, the contributions of NO_x are indirect and dependent on the emission altitude. NO_x results in the formation of short-term ozone, resulting in a heating or positive radiative forcing effect, and the depletion of methane and primary-mode ozone, having an opposite effect. Nevertheless, the current net impact of NO_x on radiative forcing is expected to be positive.

Contrails are formed when the hot and moist jet of the engine mixes with the cold, dry ambient air, provided certain conditions are met. The aircraft has to fly through an ice super-saturated region and the Schmidt-Appleman criterion has to be satisfied. Although soot aerosols are not considered in these formation criteria, they do perform an important role in the radiative properties of contrails. Since soot aerosols provide nuclei to form droplets, the soot concentration in the exhaust determines the ice crystal number and crystal size. These features in turn affect the optical depth and lifetime of the contrails, thereby influencing the radiative forcing.

The contributions of these different climate agents are translated to radiative forcing in the linearized climate model [25, 26]. The radiative forcing is then normalized with respect to the radiative forcing due to a doubling in atmospheric CO_2 concentration, and summed according to their respective climate sensitivities. The temperature response then follows from a convolution integral over the period under investigation, where the response function models the climate's response to the radiative forcing [26]. For kerosene-powered aircraft, the required calculations are described in Reference [16].

SAF The major climate impact reduction from SAF arises from the reduction in net CO_2 emissions. Since such fuels are derived from biomass or waste products, no new carbon is introduced in the global carbon cycle [4]. Hence, although combustion in engines still produces CO_2, the net effect on a global scale can be close to zero, depending on other phases in the lifetime of these fuels [3]. If we purely consider the impact of in-flight CO_2 emissions, this impact can be assumed to be zero, i.e. carbon-neutral flight [27].

The NO_x emissions and their effects remain unchanged for SAF. This is because the NO_x production results from the combustion characteristics, such as flame temperature and speed, which are similar for kerosene and SAF. The study by Moore et al. [28] also confirms that the NO_x emissions are similar for Jet-A fuel and a 50:50 blend of HEFA and Jet-A.

On the other hand, the use of SAF is expected to lower the radiative impact due to contrails, while the slightly higher water content can lead to the more frequent formation of contrails near-threshold conditions [21]. The reduction in radiative forcing arises from the lower aromatics content in biofuels. These aromatics are precursors for soot [10]. Lower soot emissions lead to a lower amount of condensation nuclei. In turn, this leads to a lower ice crystal number and larger crystal size. This larger crystal size also performs a role during the vortex phase of the contrails, where more ice particles are expected to survive [21, 29]. Nevertheless, the lower ice crystal number and larger size lower the optical thickness of contrails and reduce their lifetime [6]. We assume a 50% reduction in contrail radiative forcing compared to aircraft powered fully by kerosene. This corresponds approximately to an 80% reduction in ice crystal number [6].

Hydrogen The lack of hydrocarbon molecules in liquid hydrogen is a desirable characteristic of this fuel. This eliminates the emissions of CO_2, as well as the need to capture carbon from the atmosphere. Additionally, the use of hydrogen can also improve the climate impact due to non-CO_2 agents. Firstly, it is argued that NO_x emission can be reduced. This can be achieved due to the wide flammability limits and the higher flame speeds of hydrogen [10]. Research has shown that by applying micro-mixing or lean-direct injection technologies, the NO_x emissions can be reduced by 50 to 80% compared to kerosene combustors [2, 11, 30, 31]. In this study, we assume that hydrogen combustion results in a 65% reduction of NO_x per unit of energy.

Secondly, hydrogen combustion affects contrail formation and properties. The higher water content in the exhaust makes saturation with respect to liquid more probable, leading to more frequent contrail formation, possibly at lower altitudes. On the other hand, the absence of soot particles in the exhaust leads to a reduction in nuclei to form droplets. Although contrails are still formed due to ambient aerosol particles, research indicates that the ice crystal number can be reduced, leading to larger ice crystal [9, 11]. Similar to the reasoning introduced above, this lowers the radiative forcing of the contrails. Assuming an order of magnitude difference in ice particle number, a decrease in radiative forcing due to contrails of 70% per kilometer of persistent, linear contrails is assumed, compared to kerosene. In conclusion, it is expected that contrails form more frequently, but have a lower radiative if hydrogen is used.

5. Cost

The second optimization objective is the cash operating costs (COC). In the current analysis, the cash operating costs consist of flight costs, namely fuel, oil and crew, as well maintenance costs. These components make the COC dependent on cruise efficiency, flight time, and distance flown. Although operational scenarios of several decades are considered in this study, all costs are expressed in 2030 United States Dollars (USD). Other costs which are typically included in direct operating costs, such as depreciation and fees, are omitted in the current analysis to reduce the uncertainty.

At the time of writing, the fuel price of kerosene is the lowest of all three options considered. The kerosene fuel price is assumed to be 2.71 2030 USD per US gallon. The average price of jet fuel in August 2021 is taken and corrected for 2% inflation p.a. to obtain the estimate in 2030 USD. The price of liquid hydrogen is set to 4.4 USD/kg [32], or approximately 1.80 USD per gallon, although this price level is expected to further reduce in the upcoming decades. Considering sustainable aviation fuel, research from the World Economic Forum indicates that HEFA-SPK will cost approximately 1159 USD per ton, or 3.53 USD per gallon, in 2030 [4]. The price estimate of synthetic kerosene is higher at 1967 USD per ton. In this research, we use the price estimate for HEFA-SPK for the initial optimizations.

The costs associated with the cabin crew, consisting of a captain, first officer, and cabin attendants, as well as the cost for maintenance, are modeled according to the methods laid out by Roskam [33]. The number of flight attendants per flight amounts to at least one cabin crew member per 35 passengers. The assumed salaries for on-board and maintenance personnel represent the average salaries in the United States in 2020 and 2021, correct for annual inflation of 2% up to 2030. This approach is similar to the research in Reference [15].

C. Top Level Requirements and Future Fleet Scenarios

Three different aircraft categories are considered in this study, being regional, medium-range and long-range aircraft. Although the names are related to the range requirement, the categories also feature distinct payload specifications. Table 4 summarizes the the top-level aircraft requirements for each aircraft category. The values are taken from the Aircraft Characteristics and Airport Planning documents of the respective reference aircraft, namely the Embraer 175 [34], the Airbus A320 [35], and the Airbus A350 [36]. The landing mass factors are deduced from the maximum landing mass of the aircraft. For hydrogen aircraft, we assume that the landing mass factor is larger because the fuel is lighter.

Table 4 Top-level aircraft requirements employed for the aircraft design [34–36]

Requirement [Unit]	Regional	Medium-Range	Long-Range
Maximum structural payload $m_{\text{pl,max}}$ [metric tons]	10.1	18.2	54.0
Harmonic range r_{harm} [km (nm)]	2410 (1300)	3200 (1730)	10800 (5830)
Ferry range r_{ferry} [km (nm)]	4630 (2500)	6750 (3645)	18000 (9720)
Approach speed v_{app} [m/s (kts)]	69.0 (134)	70.0 (136)	72.0 (140)
Take-off length (ISA conditions) [m (ft)]	1700 (5580)	2100 (6890)	2700 (8860)
ICAO Reference Code	3C	4C	4E
Maximum span b_{max} [m]	36.0	36.0	65.0
Diversion range r_{div} [km (nm)]	185 (100)	463 (250)	463 (250)
Loiter time t_{hold} [min]	45	35	35
Landing mass factor f_{W} kerosene and SAF [-]	0.91	0.88	0.73
Landing mass factor f_{W} hydrogen [-]	0.97	0.94	0.87
RPK 2050 [pax km / year]	2.98×10^{11}	3.95×10^{12}	1.21×10^{12}
Reference block range r_{bl} [km (nm)]	894 (483)	1852 (1000)	6060 (3270)
Reference load factor (passengers) [-]	0.80 (67)	0.72 (130)	0.58 (253)

We assess the climate impact using the average temperature response over 100 years starting in 2020, although this point is chosen arbitrarily. In this period, the aircraft are introduced into the market from 2020 onward, are operated for 35 years, and are retired. The annual aircraft production is constant and ends in the year 2050. This means that the fleet size increases linearly from 2020 to 2050, is constant between 2050 and 2055, and reduces linearly until the complete fleet is retired in 2085.

The fleet size reaches its maximum in 2050 and the number of operational aircraft depends on the productivity level set, similar to the approach taken in References [15, 16]. This productivity level is expressed as the revenue passenger kilometers (RPK) per year, for a given aircraft category. These productivity levels in the year 2050 are derived from data in the United States provided by the Bureau of Transport statistics, the Airline Data Management project [37], and the Regional Airline Association [38]. For each category, we assume a 2 to 3% annual growth in RPK until 2050, yielding the projections provided in Table 4. Furthermore, it is imposed that the entire demand is covered by the newly introduced, optimal aircraft. The summary tables in Appendix B indicate the total aircraft produced for each category, depending on the optimization case.

To estimate the emissions and subsequently the climate impact, a reference mission is assumed for each aircraft type. These missions are defined by the passenger load factor and stage length in Table 4 and represent the average mission flown in the aircraft category. The chosen load factor and block range are derived from transport data in the past decade [37, 38]. These reference missions lie well-inside inside the respective payload-range envelopes and are not the constraining design missions.

III. Verification

The majority of the above design methods have been verified in previous research [15, 16]. This verification includes the physics-based thermodynamic analysis and design of the engines, both for kerosene- and hydrogen-powered aircraft, and the aircraft design convergence for medium-range and long-range aircraft. No additional verification is required for the SAF-powered engines since we evaluate these engines with the verified kerosene gas model. Only the mass estimation, geometry prediction, and performance calculations have to be evaluated for the regional aircraft.

The Embraer 175 serves as the reference aircraft to verify the design methods for regional aircraft. The assumed top-level requirements are equal to the ones provided for regional aircraft in Table 4. The geometric parameters for the regional aircraft in Table 2 are used to model the Embraer 175. Appendix A summarizes the engine design variables and component efficiencies. Due to the lack of CF34-8E component efficiencies, these parameters are assumed similar to those of the CFM56 which powers medium-range aircraft such as the Airbus A320. Further details on this engine can be found in Table 12 in the appendix.

Table 5 compares the main mass groups and geometric features of the modeled aircraft with data of the Embraer 175 [34]. We deem these relative differences acceptable for the current design analysis. Figure 2 also indicates that the fuselage geometry and wing planform match well with those of the real aircraft. This means that the geometric and performance assumptions allow the accurate modeling of the aircraft. We determine the wing position by assuming that the OEM center-of-gravity lies at approximately 35% of the mean aerodynamic chord. Of course, this assumption relies on a conceptual estimation of the masses and relative position of the different structural groups, namely the fuselage, engines, wing, empennage, furnishing, and systems.

Table 5 Validation of aircraft design modules for Embraer 175 [34]

Parameter [Unit]	Framework	Reference	Difference [%]
MTOM [metric tons]	37.1	37.5	-1.0
OEM [metric tons]	21.2	21.5	-1.6
Fuel Mass m_{fuel} [metric tons]	5.78	5.80	-0.3
Wing area S [m]	72.2	72.7	-0.7
Wing span b [m]	24.9	26.0	-4.2
Outer fuselage diameter $d_{\text{fus,outer}}$ [m]	2.98	3.01	-1.0
Fuselage length l_{fus} [m]	31.6	31.7	-0.3

Figure 3 compares the simulated payload-range diagram to the actual diagram of the Embraer 175 aircraft. Up to the payload-range combination where the maximum usable fuel is reached, the diagram and slope correspond well to the actual performance. Beyond this point, between approximately 3600 km and the ferry range, it appears the range gained due to payload removal is underestimated. Since the slope prior to this section is modeled correctly, we hypothesize that the cause of this offset is a difference in reserve-fuel calculation or strategy.

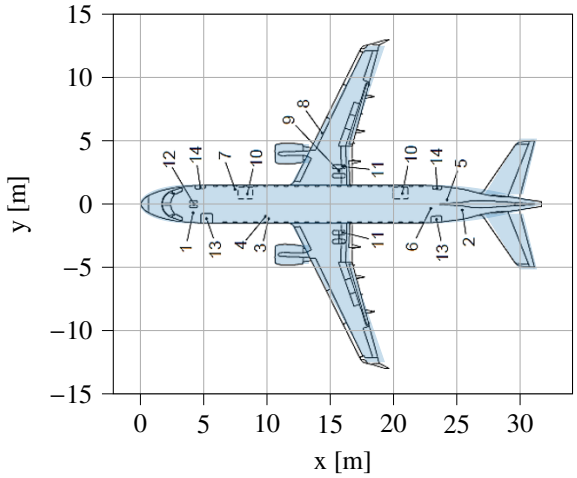

Fig. 2 Verification of Embraer 175 top view geometry (black lines correspond to actual geometry [34], blue shaded shape is the modeled aircraft)

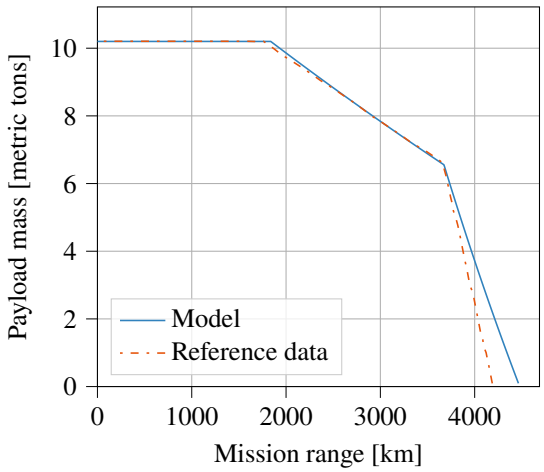

Fig. 3 Verification of Embraer 175 payload-range diagram [34] (M_{cr}=0.78, h_{cr}=10.7 km)

IV. Results and Discussion

We employ the methodology from Section II to perform the multidisciplinary design optimizations for the three fuel types and aircraft categories. The results for each aircraft type consist of the optimized objective values and design vectors for each fuel type, as well as a comparison of the temperature response. Additionally, the trade-off between the cost and climate design objectives is studied for all fuel types simultaneously by plotting the Pareto fronts, using the kerosene, cost-optimal aircraft as reference cases. Section V.B provides more insight into the features of each optimized aircraft. Furthermore, a comparison of different SAF mixtures and the influence on the COC is presented in Section IV.D

A. Regional Aircraft

Although the regional aircraft market segment is smaller than that of medium-range aircraft, this category still performs an important role. From the optimizations, we observe that a significant reduction of up to 71% in ATR_{100} is possible using kerosene. This result and the optimized objective values for other fuels are presented in Table 6. To achieve this climate-impact saving with kerosene, the aircraft is designed to fly at an altitude of 6 km and a Mach number of 0.6, as summarized in Table 7. These two design variables reach the lower bounds of the design space. The slower flight and longer block time increase the cash operating costs by approximately 3%. Compared to the other categories, this cost penalty is limited since the regional aircraft has a short cruise phase. Therefore, the reduction in block speed has a low effect on time-driven cash operating costs compared to the medium- and long-range categories.

Table 6 Optimized objective function values for the regional aircraft. The objective names in the column headers are the objectives for which the aircraft are optimized. The rows show the relative changes in the parameters identified the leftmost column.

	Kerosene		**Hydrogen**		**SAF - HEFA**	
Variable	**ATR_{100}**	**COC**	**ATR_{100}**	**COC**	**ATR_{100}**	**COC**
ATR_{100}	-71%	-	-99%	-66%	-86%	-47%
COC	+4.8%	-	+30%	+26%	+7.9%	+3.2%
E_{fuel}	-3.2%	-	+8.0%	+4.5%	-2.0%	0%

When SAF is used in regional aircraft, the average temperature response can be reduced by 47% if the aircraft is optimized for costs, and 86% if the climate-optimal solution is taken. As can also be observed in Figure 6, a redesigned

kerosene aircraft would be preferred to a SAF-powered aircraft since it can provide a similar climate impact reduction at a lower cost increase. Liquid hydrogen can provide the largest ATR_{100} reduction (99%) of all three fuels if the climate objective is prioritized over the costs in the design. Due to the tank integration, the energy consumption increases up to 8%. This, together with the high fuel price, leads to a 30% in costs compared to the cost-optimal, kerosene aircraft, as can be seen in Table 7.

Table 7 presents the design variables corresponding to the optimized objectives in Table 6. When switching from the COC objective to ATR_{100}, all aircraft fly lower and slower, have a higher wing loading, and feature a lower fan pressure ratio. The lower fan pressure ratio is accompanied by a higher bypass ratio for the climate-optimal alternatives.

The kerosene and SAF aircraft exhibit similar design strategies, despite minor offsets in the optimal design variables which are believed to result from the numerical optimization. When we compare these aircraft to the hydrogen alternative, several observations can be made. First, the cost-optimal hydrogen aircraft cruises slower and higher. This is because the costs are driven by the fuel price, requiring a more energy-optimal solution rather than one which minimizes the time-driven costs. The need for an energy-optimal solution is also confirmed by the higher aspect ratio. Although this raises the wing mass, the lower sweep angle limits the mass penalty. Secondly, when moving from the cost objective to the climate one, the trend in TET appears to be opposite for the hydrogen concept compared to the kerosene and SAF solution, where the TET decreases. Furthermore, the hydrogen aircraft always reach the maximum wing loading constraint, whereas the optimizer sometimes chooses a lower W/S for the kerosene and SAF aircraft to favor a lower thrust-to-weight ratio T/W in take-off.

Table 7 Optimized design variables for the regional aircraft. The objective names in the column headers are the objectives for the which the corresponding variables are optimized. The bars at the bottom or top of numbers indicate that lower or upper bounds, respectively, are reached.

	Kerosene		**Hydrogen**		**SAF**	
Variable [Unit]	**ATR_{100}**	**COC**	**ATR_{100}**	**COC**	**ATR_{100}**	**COC**
A [-]	11.8	7.95	10.9	$\overline{12.0}$	11.4	8.31
W/S [kN/m^2]	5557	5315	5545	5329	5637	5431
BPR [-]	9.80	7.50	9.35	8.00	8.45	5.89
Π_{fan} [-]	1.48	$\overline{1.80}$	1.59	$\overline{1.80}$	1.53	$\overline{1.80}$
Π_{lpc} [-]	1.61	1.48	1.79	1.68	1.56	1.33
Π_{hpc} [-]	23.7	22.4	21.1	19.8	$\overline{25.0}$	$\overline{25.0}$
TET [10^3 K]	1481	1516	1504	1450	1489	1425
h_{cr} [km]	$\underline{6.00}$	9.75	$\underline{6.00}$	10.4	$\underline{6.00}$	9.77
M_{cr} [-]	$\underline{0.60}$	0.78	$\underline{0.60}$	0.71	$\underline{0.60}$	0.77

One can compare the different geometries of the regional aircraft concepts in Figure 4. For both the cost and climate objectives, it is clear that the kerosene- and SAF-powered aircraft are nearly identical. The hydrogen aircraft, on the other hand, features a longer fuselage to facilitate room for the tank. This integration elongates the fuselages by 3.1 m in the case of cost-optimal aircraft, and by 3.8 for the climate-optimal alternative. A larger tank is required for the climate-optimal solution due to its higher energy consumption. Furthermore, the cost-optimal, hydrogen aircraft flies at a lower Mach number and therefore has a lower wing sweep angle compared to the other fuels. The larger MTOM of the hydrogen aircraft also leads to a larger wing surface which extends the wing span up to 27 m.

The ATR_{100} objective is computed from the mean surface temperature response over the 100-year period considered in the hypothetical scenario. While the ATR offers an overall evaluation of the climate impact, the temperature response yields more insight into the timeline of the climate impact due to the fleet operation. Figure 5 presents the temperature response for the cost- and climate-optimal design, considering different fuels. Comparing Figure 5b to Figure 5a, one can deduce that mainly the short-term, hence non-CO_2, effects are reduced by flying lower and slower. The difference between the kerosene and SAF responses is due to the altered contrail properties and CO_2 reduction. The response of SAF is lowered further by switching to hydrogen because CO_2 are eliminated and NO_x emissions are reduced. Nevertheless, the contribution due to H_2O is higher for the hydrogen aircraft.

In Figure 6 we study the trade-off between cash operating costs and climate impact reduction for the different fuels

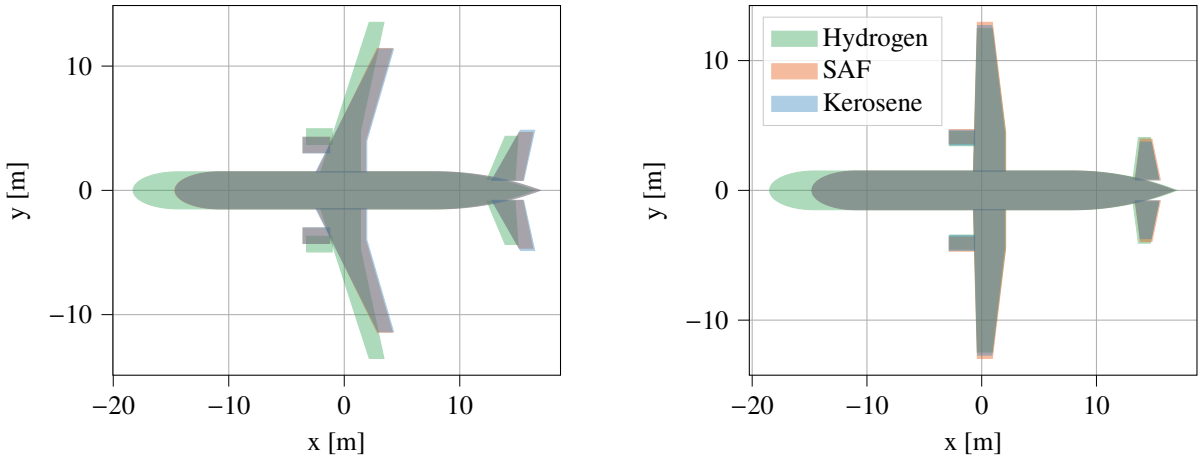

(a) Cost-optimal **(b) Climate-optimal**

Fig. 4 Comparison between top-view geometries of cost- and climate-optimal, regional aircraft employing different fuel types

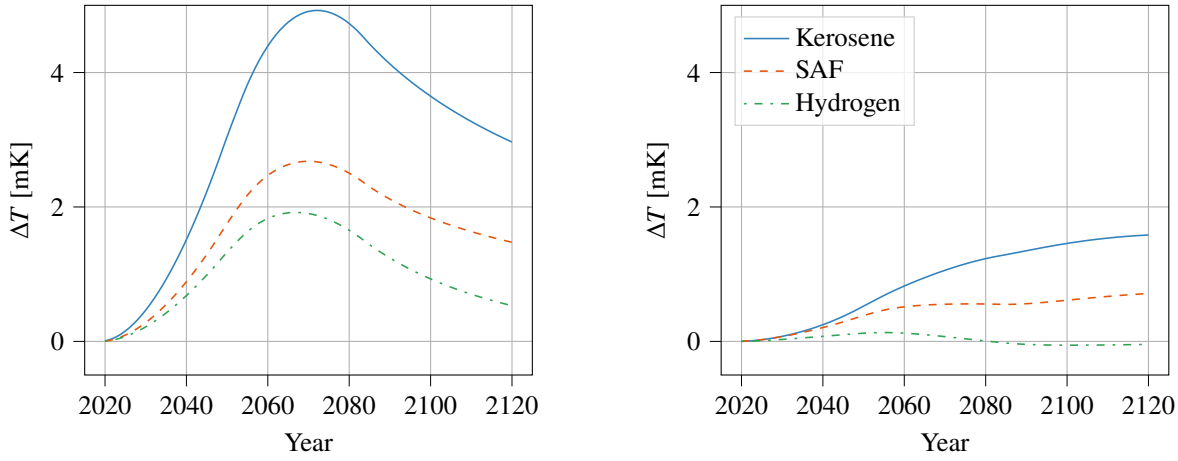

(a) Cost-optimal **(b) Climate-optimal**

Fig. 5 Comparison between mean surface temperature responses of cost- and climate-optimal, regional aircraft employing different fuel types

in the regional aircraft category. The kerosene-powered would allow a significant climate impact reduction of 69% before the SAF aircraft becomes Pareto-optimal. SAF can reduce the climate impact further, up to 86% for an 8% increase in costs. The maximum climate impact reduction is achieved with liquid hydrogen. However, only the design solutions close to the climate-optimal hydrogen design appear to be Pareto-optimal. This indicates that, for the regional market, SAF aircraft are preferred to hydrogen aircraft optimized for costs.

B. Medium-Range Aircraft

Table 8 presents the objective values for the optimized medium-range aircraft, relative to the the kerosene, cost-optimal aircraft. While a reduction of 64% in ATR_{100} can be realized with kerosene aircraft, the potential savings with SAF and hydrogen are larger. As shown in the table, sustainable aviation fuels (here HEFA and kerosene mixture) can offer a reduction between 47 and 82%, for a cash operating cost increase of 5 to 14%. Along with this decrease in ATR_{100}, the in-flight energy consumption (E_{fuel}) reduces marginally due to the higher LHV of SAF.

The hydrogen aircraft offer the largest climate impact reduction potential for the hypothetical fleet, up to 99%. This almost climate-neutral solution follows from the elimination of CO_2 emissions and contrail formation. The remaining

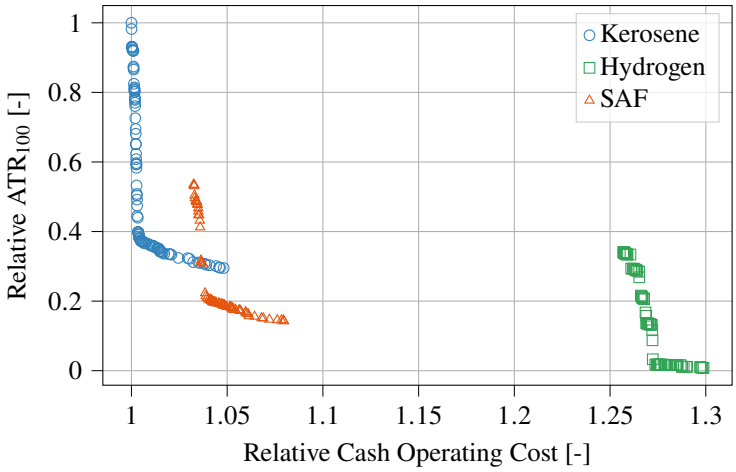

Fig. 6 Comparison of Pareto-optimal solutions for regional aircraft. All values are presented relative to the cost-optimal, kerosene aircraft.

Table 8 Optimized objective function values for the medium-range aircraft. The objective names in the column headers are the objectives for which the aircraft are optimized. The rows show the relative changes in the parameters identified the leftmost column.

	Kerosene		Hydrogen		SAF - HEFA	
Objective	**ATR_{100}**	**COC**	**ATR_{100}**	**COC**	**ATR_{100}**	**COC**
ATR_{100}	-64%	-	-99%	-71%	-82%	-47%
COC	+8.1%	-	+42%	+33%	+14%	+5.1%
E_{fuel}	-0.2%	-	+14%	+3.7%	-0.4%	-1.6%

contributions are NO_x effects and H_2O emissions. However, this climate impact reduction is accompanied by a 42% increase in cash operating costs and a 14% increase in in-flight energy consumption. More energy is required due to the increased mass and drag as a result of the tank integration. The larger energy requirement and higher fuel costs lead to the significant increase in COC.

Table 9 presents the design variables corresponding to the optimal solutions introduced above in Table 8. When moving from the cost to the ATR_{100} objective, the variation in cruise altitude, Mach number, turbine entry temperature, and fan pressure ratio show similar trends for the three fuel types (An overview of all design variables is shown in Figure 10). These four parameters decrease to reduce the climate impact while being limited by the imposed constraints. First, a lower cruise altitude lowers the effects due to NO_x emissions, in particular the formation of ozone, and simultaneously lowers the impact of contrails, up to an altitude where contrails are no longer formed. This variable reaches the lower bound in all climate-optimal cases. Secondly, M_{cr} reduces alongside h_{cr} to maintain a lift-to-drag ratio in cruise close to the energy-optimal value. Finally, the optimizer chooses to lower Π_{fan} and TET. We expect that this is a consequence of the higher inlet temperature at lower altitudes, as well as the constraint on TET at take-off being active. Lowering the Mach number with altitude also increases the maximum achievable $C_{L,max}$, which in turn allows a higher wing loading W/S. The optimizer makes use of this higher W/S for the kerosene and SAF aircraft.

Although the design parameters are not exactly the same, the kerosene and SAF aircraft are rather similar. This can also be seen from the top views presented in Figure 7. One difference in the cost-optimal aircraft is the cruise Mach number, which is slightly higher for the kerosene design (0.81) than for the SAF alternative (0.79). This is driven by the relative difference between fuel costs and time-driven costs, such as salaries. Since SAF is more expensive, the optimal solution flies slower to approach a more energy-optimal solution. Relatively speaking, the time-driven costs are more important for the kerosene aircraft, which requires a reduced block time and hence higher cruise speed. This difference in Mach number also causes a minor difference in wing quarter-chord sweep angle, as shown in Figure 7a.

The cost-optimal hydrogen aircraft flies slower, at Mach 0.73, at a higher initial cruise altitude than the kerosene-

Table 9 Optimized design variables for the medium-range aircraft. The objective names in the column headers are the objectives for the which the corresponding variables are optimized. The bars at the bottom or top of numbers indicate that lower or upper bounds, respectively, are reached.

	Kerosene		Hydrogen		SAF - HEFA	
Variable [Unit]	**ATR_{100}**	**COC**	**ATR_{100}**	**COC**	**ATR_{100}**	**COC**
A [-]	10.9	7.95	11.1	11.4	11.9	8.58
W/S [kN/m^2]	6201	5506	5310	5570	6030	5620
BPR [-]	8.23	8.17	8.33	9.57	8.72	8.04
Π_{fan} [-]	1.48	$\overline{1.80}$	1.55	1.76	1.43	$\overline{1.80}$
Π_{lpc} [-]	1.72	1.40	1.56	1.37	1.67	1.58
Π_{hpc} [-]	23.3	23.9	24.6	$\overline{25.0}$	$\overline{25.0}$	20.9
TET [10^3 K]	1443	1548	1450	1520	1420	1540
h_{cr} [km]	$\underline{6.00}$	10.1	$\underline{6.00}$	10.4	$\underline{6.00}$	9.95
M_{cr} [-]	$\underline{0.60}$	0.81	$\underline{0.60}$	0.73	$\underline{0.60}$	0.79

and SAF-powered aircraft. Since we are assuming a continuous climb procedure in cruise, the initial cruise altitude is partially determined by the mass loss in cruise due to fuel burn. Since the hydrogen aircraft burns less fuel mass, the initial cruise altitude is higher. Related to this reduced mass loss, the maximum landing mass of the hydrogen aircraft is higher. This limits the maximum wing loading and explains why this variable is lower than for other fuel types.

From Table 9 one may deduce that the selected bypass ratios are rather low compared to state-of-the-art engines. This is a result of the high limit on the overall pressure ratio and the bound on the TET in take-off. The optimizer increases the OPR, in particular, Π_{hpc}, which also requires a high TET. Increasing the bypass would also require a higher TET in order to extract enough energy from the turbine to power the big fan. However, TET is limited by the constraint in take-off. Hence, the optimizer appears to prefer increasing the OPR over a rise in BPR. We expect that this is because an increase in OPR results in lower drag and mass penalties than an increased bypass ratio. A recommendation for further research is therefore to include turbine cooling, which would allow higher TET without violating the 2000 K constraint, leaving more room for engines with high bypass ratios.

Figure 7 compares the top-view geometries of the kerosene-, SAF- and hydrogen-powered aircraft, considering the cost and climate objectives separately. The fuselage of the hydrogen aircraft is noticeably longer for both objectives because of the hydrogen tank integration in the fuselage. This long fuselage leads to a heavier fuselage structure, larger operating empty mass, and higher zero-lift drag coefficient. These two latter effects lead to increased energy consumption. By comparing Figure 7a and Figure 7b, one can see the wing sweep angle and consequent change in horizontal tail planform are the most prominent geometric changes.

In Figure 8 we compare the mean surface temperature response for all optimal medium-range aircraft. From Figure 8a it is clear that the SAF and hydrogen solutions reduce the overall temperature response, mainly because of long-term CO_2 emissions. In addition, the short-term peak is lowered due to the altered contrail properties and, in the case of hydrogen aircraft, the reduced NO_x emissions. The lack of a peak near the year 2070 Figure 8b indicates that, by optimizing the aircraft for their climate impact, the short-term effects from NO_x and contrails can be reduced, irrespective of the fuel. A long-term CO_2 contribution remains in the year 2120 for the kerosene and SAF aircraft.

While Table 8 shows the results of single-objective optimizations, solutions exist which are Pareto-optimal and lie in between the extremes. Figure 9 presents the Pareto fronts for the three fuels under consideration. From this figure, we can deduce kerosene aircraft offer low-cost solutions for a climate impact reduction of 62%. After this point, SAF aircraft concepts offer the largest climate impact reduction for a given increase in costs. However, a reduction in ATR_{100} above 82% can only be achieved with hydrogen-powered aircraft. But this fuel also yields the largest cost penalty. Nevertheless, these results strongly depend on the fuel prices of SAF and hydrogen in the future.

Figure 10 shows how the design variables vary along the Pareto fronts in Figure 9. For each graph, the leftmost data corresponds to the cost-optimal solution, while the climate-optimal solutions are obtained by moving to the right. For example, the bottom two rows show how the cruise altitude and Mach number decrease when moving towards the climate-optimal solution.

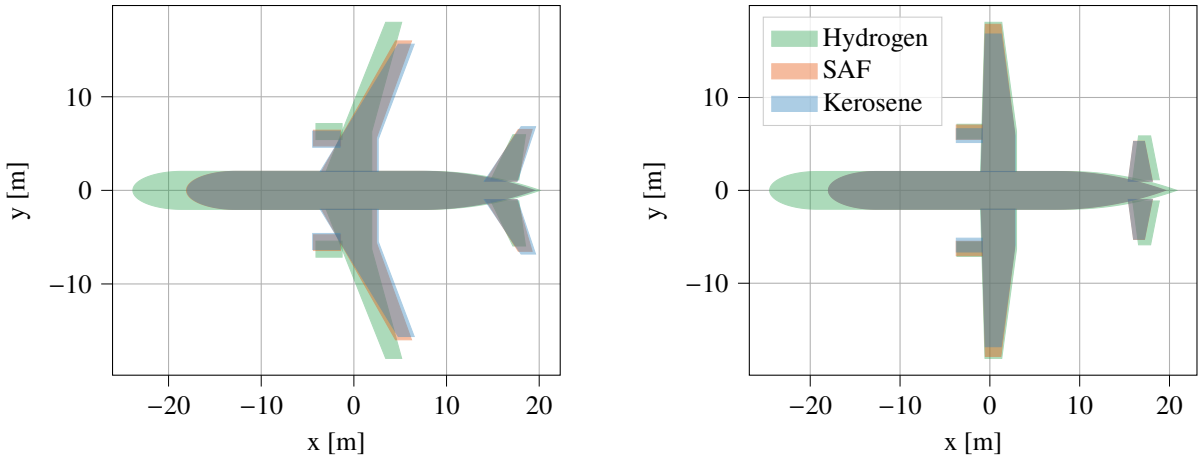

(a) Cost-optimal **(b) Climate-optimal**

Fig. 7 Comparison between top-view geometries of cost- and climate-optimal, medium-range aircraft employing different fuel types

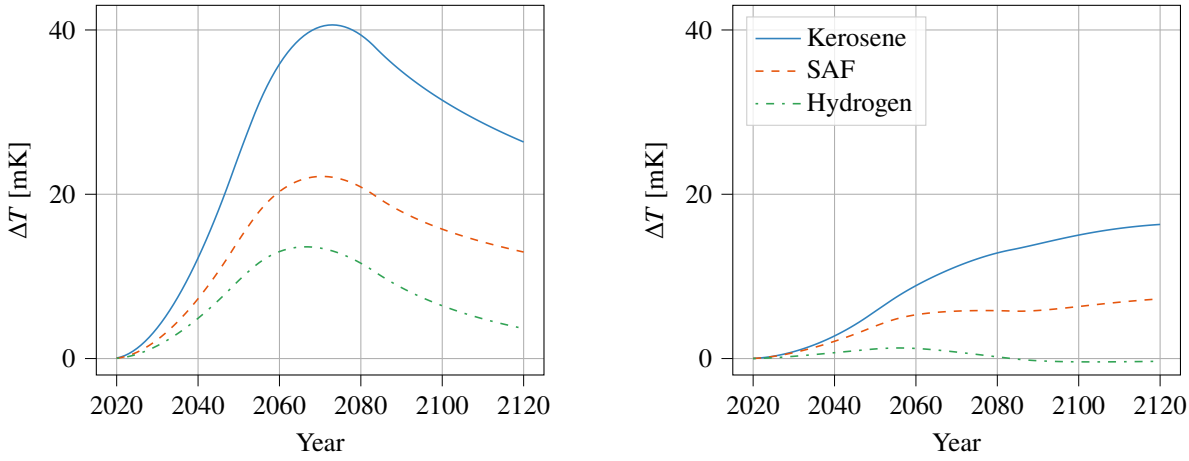

(a) Cost-optimal **(b) Climate-optimal**

Fig. 8 Comparison between mean surface temperature responses of cost- and climate-optimal, medium-range aircraft employing different fuel types

C. Long-Range Aircraft

Finally, we present the results for the long-range aircraft category. Table 10 shows the objective function values for the aircraft designed for different objectives and different fuel types. The possible ATR_{100} reduction for the kerosene aircraft has shrunk to 46%, whereas it was 71 and 64% for the regional and medium-range aircraft. This is because the relative contributions of the different climate agents change between categories. In the long-range category, the CO_2 emissions are relatively more important for the cost-optimal aircraft. However, the CO_2 cannot be reduced as much as the other contributions. For the other categories, the contribution due to contrails is larger in the cost-optimal case, and hence, when switching to the climate objective, a larger reduction can be achieved.

When burning SAF or hydrogen, the climate impact can be significantly improved by up to 72 and 98%. Comparing the climate-optimal kerosene and SAF solutions, it seems that the SAF concept is interesting because, for a cost increase of 26 instead of 21%, the ATR_{100} can be reduced by 72 instead of 46%. The application of hydrogen fuel yields the largest potential since CO_2 emissions perform an important role for long-range aircraft. Nevertheless, the long-range flight and its corresponding energy usage require a large tank, which strongly penalizes the energy consumption of long-range aircraft, up to 24%. Although hydrogen is the most attractive option from a climate-point perspective, this

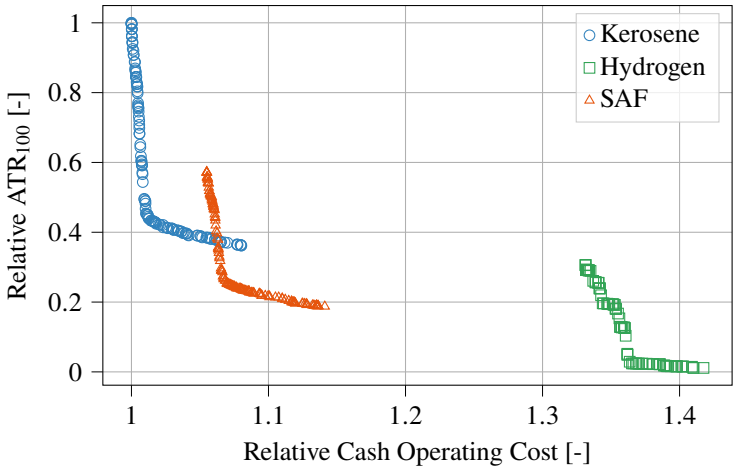

Fig. 9 Comparison of Pareto-optimal solutions for medium-range aircraft. All values are presented relative to the cost-optimal, kerosene aircraft.

fuel causes a 50 to 70% increase in cash operating costs, as indicated in Table 10.

Table 10 Optimized objective function values for the long-range aircraft. The objective names in the column headers are the objectives for which the aircraft are optimized. The rows show the relative changes in the parameters identified the leftmost column.

	Kerosene		Hydrogen		SAF - HEFA	
Variable	**ATR_{100}**	**COC**	**ATR_{100}**	**COC**	**ATR_{100}**	**COC**
ATR_{100}	-46%	-	-98%	-81%	-72%	-45%
COC	+21%	-	+69%	+49%	+26%	+5%
E_{fuel}	0%	-	+24%	+16%	0%	+2%

To achieve the climate-optimal solutions, the design variables shown in Table 11 should be applied. Similar to the two other categories, the trend is to fly lower and consequently slower to reduce the climate impact. However, the time driven-costs perform a more important role in the long-range category. This drives the Mach number in the case of the cost-optimal aircraft. When flying slower, Table 15 shows that the mission block time increases from 7h41m to 10h13m for the kerosene aircraft, a rise of 32%. This explains why the cost penalty for long-range aircraft is larger than for regional or medium-range concepts.

Furthermore, Table 11 shows that the optimizer tries to achieve maximum energy efficiency for the ATR_{100}-optimal aircraft by pushing A, BPR, and Π_{hpc} to the upper bounds of the design space. Along with the high BPR, the fan pressure ratio is lowered which also prevents the violation of the OPR constraint. This indicates that for the long-range category, high-aspect-ratio wings and high bypass ratios are required to reduce the climate impact. The wing loading constraint is not active for the kerosene and SAF aircraft, indicating that a slightly lower T/W in take-off is preferred. The hydrogen aircraft does reach the wing loading and span constraints.

The top-view geometries of the long-range aircraft are compared in Figure 11. The most obvious feature is the fuselage length of the hydrogen aircraft. The length is increased from 65 m to approximately 90 m to facilitate the tank integration, which makes the aircraft longer than the Airbus A380 and A340 aircraft (see Table 15 for more information). Possibly, this long fuselage prohibits the operation of this aircraft with current airport facilities.

Figure 12 compares the global, mean surface temperature responses for the six optimized long-range aircraft. The responses are similar to the results found for the two smaller aircraft categories, with a significantly lower temperature response for the SAF and hydrogen aircraft. Also, by selecting ATR_{100} as the optimization objective, the peak caused by short-term climate effects disappears. The relevance of CO_2 emissions on long-distance routes can be recognized in Figure 12a where the peak for kerosene and SAF powered aircraft occurs later than for the hydrogen concept. This is

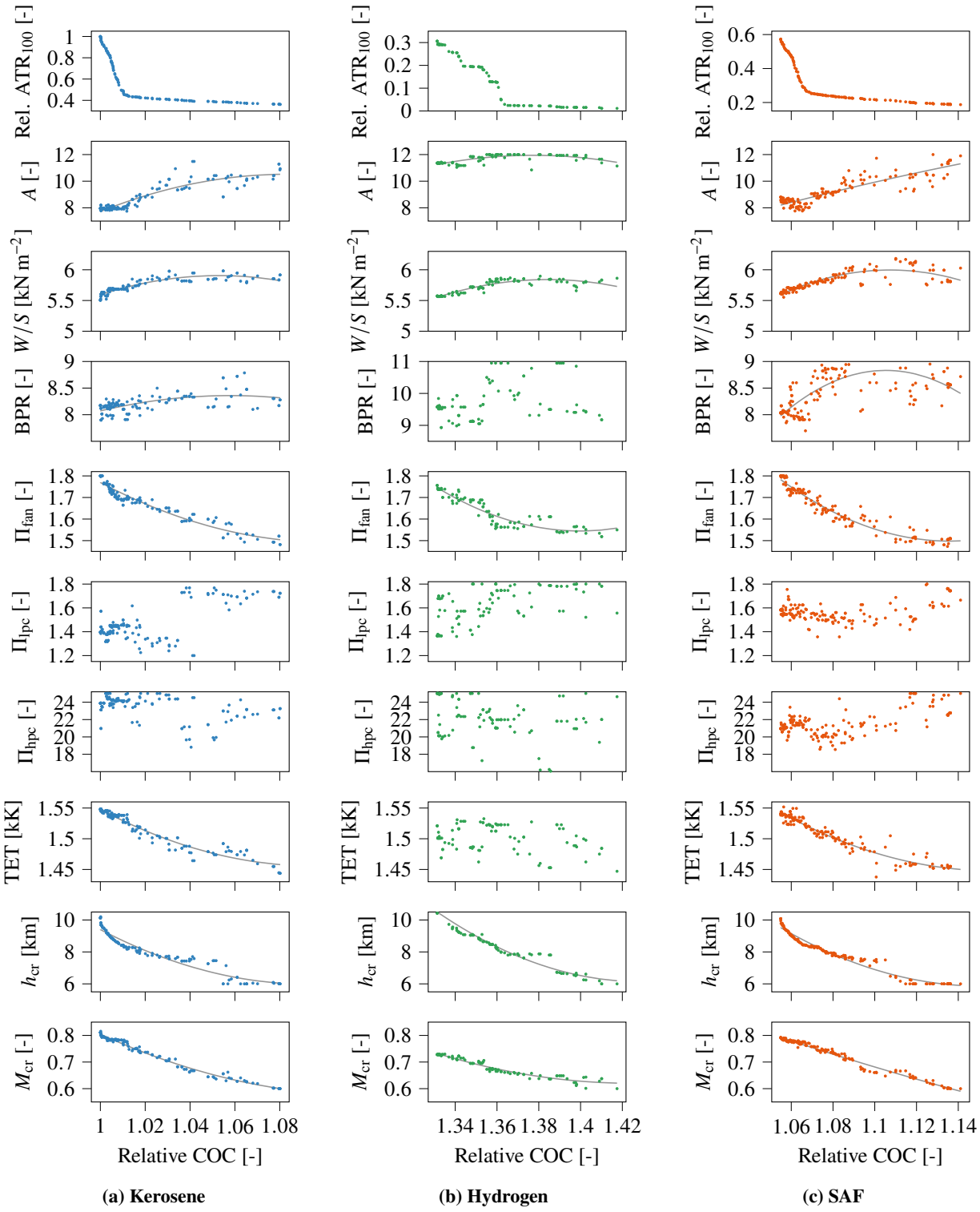

Fig. 10 Variation in design variables (second to last rows) along Pareto fronts (shown in the top row) for medium-range aircraft. A gray, polynomial trend line is added to the plot if a clear correlation exist between the objectives and the variable.

Table 11 Optimized design variables for the long-range aircraft. The objective names in the column headers are the objectives for the which the corresponding variables are optimized. The bars at the bottom or top of numbers indicate that lower or upper bounds, respectively, are reached.

	Kerosene		Hydrogen		SAF - HEFA	
Variable [Unit]	**ATR_{100}**	**COC**	**ATR_{100}**	**COC**	**ATR_{100}**	**COC**
A [-]	$\overline{12.0}$	8.00	$\overline{12.0}$	11.1	$\overline{12.0}$	8.00
W/S [kN/m^2]	7396	6612	6780	6391	7646	6652
BPR [-]	$\overline{11.0}$	10.1	$\overline{11.0}$	$\overline{11.0}$	$\overline{11.0}$	8.82
Π_{fan} [-]	1.38	1.72	1.47	1.65	1.37	1.65
Π_{lpc} [-]	1.70	$\overline{1.80}$	1.76	1.66	1.62	1.27
Π_{hpc} [-]	$\overline{25.0}$	19.1	23.1	21.9	$\overline{25.0}$	23.0
TET [10^3 K]	1454	1605	1484	1556	1436	1459
h_{cr} [km]	6.11	10.8	$\underline{6.00}$	9.35	$\underline{6.00}$	10.4
M_{cr} [-]	$\underline{0.60}$	$\overline{0.90}$	$\underline{0.60}$	0.73	$\underline{0.60}$	0.88

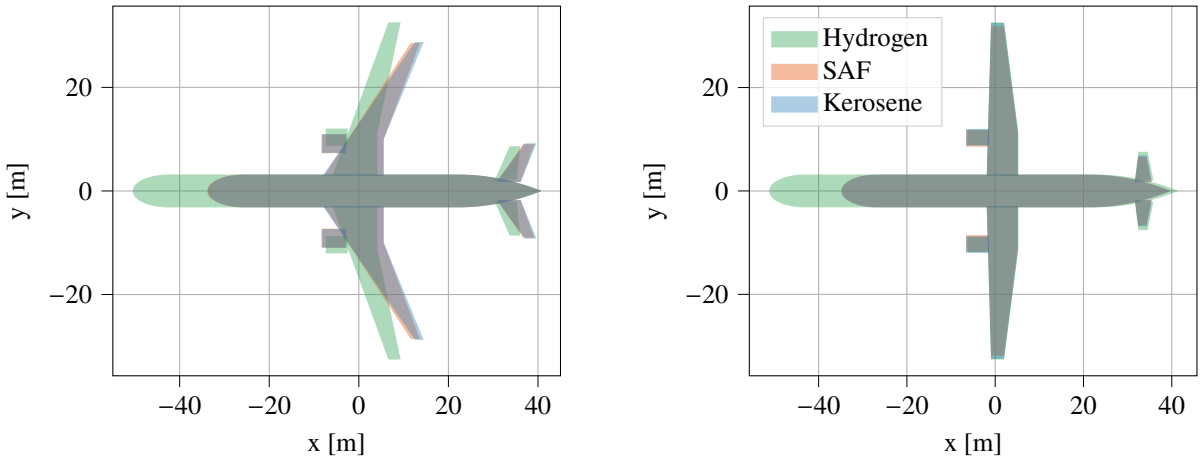

(a) Cost-optimal **(b) Climate-optimal**

Fig. 11 Comparison between top-view geometries of cost- and climate-optimal, long-range aircraft employing different fuel types

indicative of a long-term, warming effect, namely the significant contribution of CO_2 emissions.

Figure 13 presents the Pareto-optimal points in the trade-off between cost and climate impact for the long-range aircraft. Similar to the smaller aircraft categories, it is clear that SAF aircraft provide Pareto-optimal solutions at a climate impact reduction which is not achievable with kerosene. Also here the hydrogen alternative yields the largest potential ATR_{100} reduction. However, compared to the trade-offs for the other categories in Figures 6 and 9, the maximum achievable ATR_{100} savings with kerosene and SAF are limited to 46 and 72%, respectively. This makes the hydrogen, cost-optimal aircraft Pareto-optimal.

D. Sensitivity to SAF Types and Mixture

In the results above, we have assumed a 50% mixture of HEFA and traditional kerosene for sustainable aviation fuel. Nevertheless, different types of SAF are currently being researched and, once regulations change and challenges regarding the aromatic content are overcome, a higher percentage of SAF may be used. To study the effect of these alternatives on the relative cost difference between kerosene and hydrogen, we consider two other SAF alternatives: first, a mixture of 50% synthetic kerosene (power-to-liquid) and 50% traditional kerosene, and secondly, a mixture of 100%

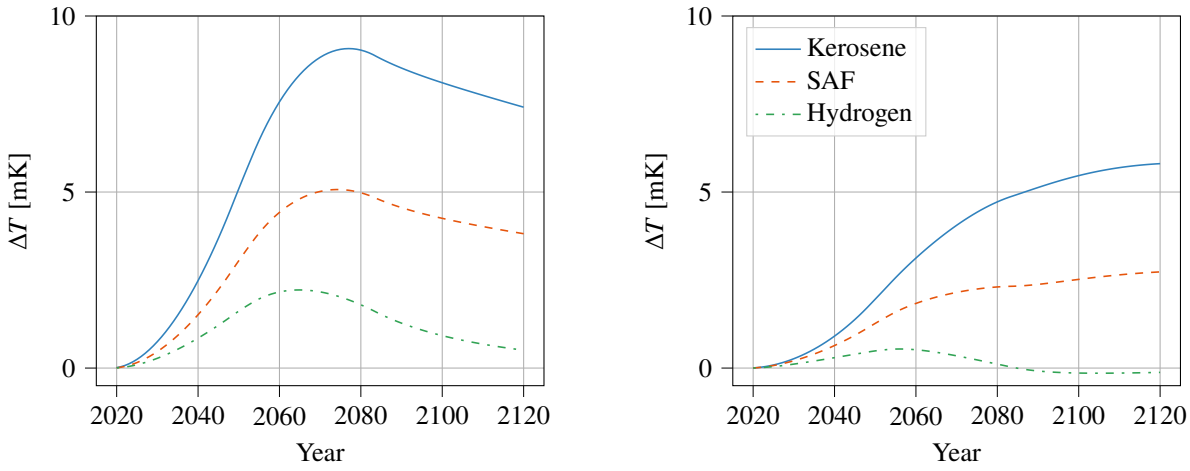

(a) Cost-optimal **(b) Climate-optimal**

Fig. 12 Comparison between temperature responses of cost- and climate-optimal, long-range, aircraft employing different fuel types

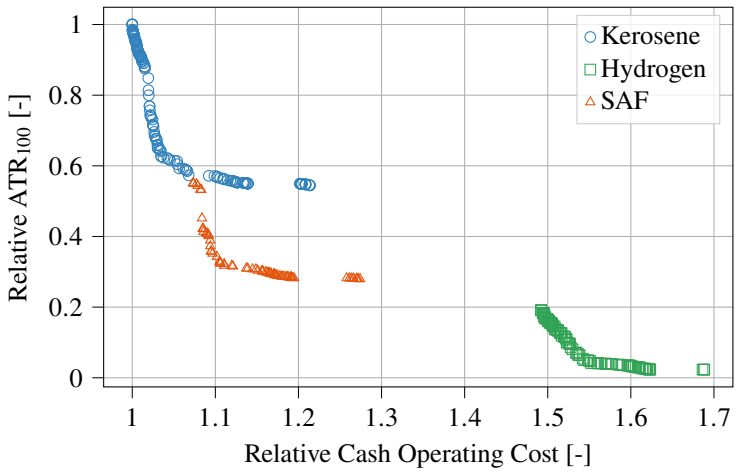

Fig. 13 Comparison of Pareto-optimal solutions for long-range aircraft. All values are presented relative to the cost-optimal, kerosene aircraft.

synthetic kerosene.

We compare these alternatives in Figure 14 for medium-range aircraft. It can be observed that the achievable Pareto front of SAF shifts to the right, indicating higher operating costs. While the 50% mixture with synthetic kerosene is still dominating the hydrogen, cost-optimal solution, the 100% synthetic jet fuel concepts are no longer Pareto-optimal. This indicates that hydrogen can provide a competitive solution if a complete carbon-neutral solution is required, especially if the liquid hydrogen price decreases.

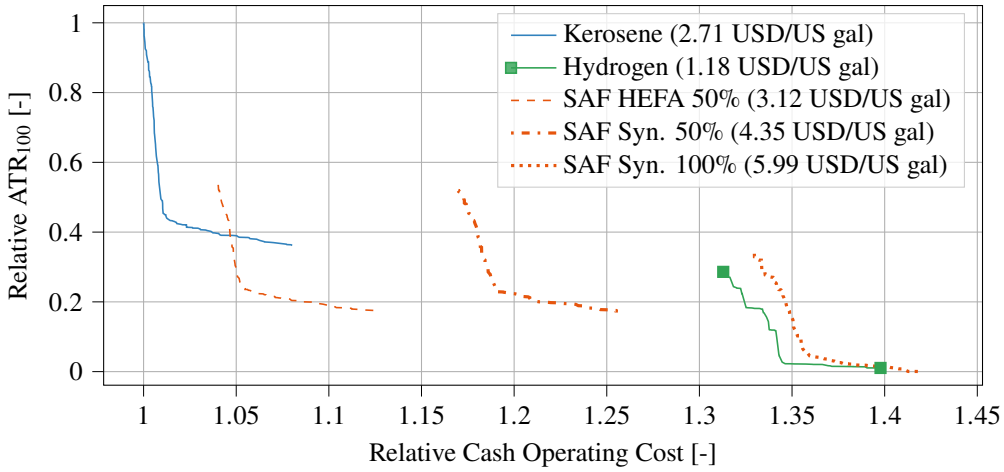

Fig. 14 Comparison of Pareto-optimal solutions for medium-range aircraft considering the influence of SAF prices. All values are presented relative to the cost-optimal, kerosene aircraft.

V. Conclusion

The objective of this research was to compare the climate impact reduction potential of several aviation fuels for three commercial aircraft categories: regional, medium-, and long-range. The fuels under consideration were traditional kerosene, liquid hydrogen, and sustainable aviation fuel (SAF). The cost-optimal, kerosene-powered aircraft provided the reference case for all multidisciplinary aircraft design optimizations. By considering both the cash operating costs and ATR_{100} as optimization objectives, we were able to study the cost versus climate trade-off for all the three fuel types in the three categories.

In all three market segments, the hydrogen-powered aircraft offer the greatest ATR_{100} reduction potential, up to 99%. This is due to the elimination of CO_2 emissions, the reduction in NO_x effects, and the lack of contrail formation by flying lower (h_{cr}=6.0 km) and slower (M_{cr}=0.6). For the regional and medium-range categories, the climate-optimal SAF aircraft design (50% HEFA or synthetic kerosene blends) can offer a similar ATR_{100} reduction as the cost-optimal hydrogen aircraft at lower cash operating costs. For the long-range aircraft, where CO_2 contributions perform a dominant role in the climate impact, cost-optimal hydrogen aircraft do provide a Pareto-optimal solution when costs and climate impact are considered. Nevertheless, the cash operating costs of hydrogen aircraft increase by 30 and 40% for regional and medium-range aircraft. For long-range missions, the operating costs rise between 50 and 70% due to the fuel price and the tank integration penalty.

We estimate that the use of SAF mixtures (50-50 with fossil kerosene) can lower the climate impact between 47 and 86-82% for regional and medium-range aircraft, whereas a maximum reduction of 72% can be achieved for long-range aircraft. The application of SAF reduces the climate impact because less carbon is added to the existing global carbon cycle and because the contrail properties are different due to lower soot production. In the case of a HEFA fuel mixture, the cash operating cost penalty is limited to 3-5% for the cost-optimal SAF aircraft, while it can rise up to 26% for climate-optimal compared to the standard kerosene aircraft.

A logical next step is to consider the climate impact of a fleet using all aircraft categories. Such as mixed fleet allows for considering the relative contributions of each category to the total climate impact. Based on these contributions, the allocation of different fuels in airline fleets can be further optimized.

Appendix

A. Embraer 175 Validation Inputs

This appendix summarizes the inputs for the CF34-8E engine model in Table 12. This engine model is used in the validation of the Embraer 175 regional aircraft.

Table 12 CF34-8E engine design parameters assumed for the design point (cruise). The component efficiencies are modeled after the CFM56 turbofan engine [39–41]

Parameter [Unit]	Value	Parameter [Unit]	Value
Inlet total pressure loss ΔP_T	0.98	Combustor total pressure loss ΔP_T	0.94
Bypass Ratio BPR	5.0	Combustion efficiency η_{comb}	0.99
Fan total pressure ratio Π_{fan}	1.5	Turbine entry temperature TET [K]	1250
Fan polytropic efficiency η_{pol}	0.89	HPT polytropic efficiency η_{pol}	0.86
LPC total pressure ratio Π_{lpc}	1.35	HPT mechanical efficiency η_{mech}	0.97
LPC polytropic efficiency η_{pol}	0.86	LPT polytropic efficiency η_{pol}	0.89
HPC total pressure ratio Π_{hpc}	14	LPT mechanical efficiency η_{mech}	0.97
HPC polytropic efficiency η_{pol}	0.90		

B. Aircraft Data

This appendix presents more information about the optimal aircraft designs presented in Section IV. Tables 13 to 15 summarize that data for regional, medium-range, and long-range aircraft.

Table 13 Performance and geometric data of optimized, regional aircraft.

	Kerosene		Hydrogen		SAF - Biofuel	
Variable [Unit]	**ATR_{100}**	**COC**	**ATR_{100}**	**COC**	**ATR_{100}**	**COC**
MTOM [-]	34.2	35.3	32.2	33.1	33.8	34.7
OEM [-]	19.8	20.8	20.5	21.5	19.4	20.3
S [m^2]	60	65	57	61	59	63
b [m]	26.6	22.8	24.9	27.0	25.9	22.8
$\Lambda_{0.25}$ [-]	0.0	24.7	0.0	16.7	0.0	24.1
λ [-]	0.46	0.25	0.46	0.32	0.46	0.26
l_{fus} [m]	31.6	31.6	35.5	34.7	31.6	31.6
L/D_{cr} [-]	16.0	15.6	15.0	17.4	15.9	15.8
T/W_{TO} [-]	0.31	0.33	0.31	0.31	0.32	0.34
T_{TO} [kN]	52	58	49	51	53	58
TSFC_{cr} [$10^{-5}\text{kg}/(\text{N s})$]	1.24	1.41	0.445	0.468	1.25	1.41
$\eta_{\text{ov,cr}}$ [-]	36%	39%	36%	38%	35%	38%
$N_{\text{AC, max}}$ [10^3]	4.9	4.4	4.9	4.6	4.9	4.4
t_{bl} [hrs]	2h28m	2h13m	2h28m	2h20m	2h27m	2h14m
SEC_{cr} [$10^{-4}\text{MJ}/(\text{N s})$]	5.33	6.05	5.33	5.61	5.43	6.14
Energy [MJ/(pax km)]	0.84	0.86	0.97	0.90	0.85	0.86

Table 14 Performance and geometric data of optimized, medium-range aircraft.

	Kerosene		Hydrogen		SAF - Biofuel	
Variable [Unit]	**ATR_{100}**	**COC**	**ATR_{100}**	**COC**	**ATR_{100}**	**COC**
MTOM [-]	65.5	68.9	63.6	64.5	66.0	68.1
OEM [-]	36.4	39.9	41.2	42.6	37.1	39.3
S [m^2]	104	123	118	114	107	119
b [m]	33.7	31.2	36.2	35.9	35.8	31.9
$\Lambda_{0.25}$ [-]	0.0	27.8	0.0	19.2	0.0	26.0
λ [-]	0.46	0.23	0.46	0.30	0.46	0.24
l_{fus} [m]	37.5	37.5	45.3	43.9	37.5	37.5
L/D_{cr} [-]	17.7	17.3	16.5	18.5	18.0	17.7
T/W_{TO} [-]	0.32	0.33	0.28	0.31	0.31	0.33
T_{TO} [kN]	104	111	86	98	102	110
$TSFC_{cr}$ [10^{-5}kg/(N s)]	1.26	1.42	4.51e-01	4.68e-01	1.23e	1.39
$\eta_{ov,cr}$ [-]	35%	40%	35%	39%	35%	39%
$N_{AC,\,max}$ [10^3]	16.4	13.9	16.4	15.0	16.4	14.1
t_{bl} [hrs]	3h54m	3h19m	3h54m	3h34m	3h54m	3h22m
SEC_{cr} [10^{-4}MJ/(N s)]	5.41	6.12	5.42	5.62	5.36	6.05
Energy [MJ/(pax km)]	0.63	0.62	0.74	0.64	0.62	0.61

Table 15 Performance and geometric data of optimized, long-range aircraft.

	Kerosene		Hydrogen		SAF - Biofuel	
Variable [Unit]	**ATR_{100}**	**COC**	**ATR_{100}**	**COC**	**ATR_{100}**	**COC**
MTOM [-]	264	276	244	248	262	275
OEM [-]	127	140	156	163	126	138
S [m^2]	350	410	352	381	336	405
b [m]	64.7	57.3	65.0	64.9	63.5	56.9
$\Lambda_{0.25}$ [-]	0.0	34.0	0.0	19.6	0.0	32.5
λ [-]	0.39	0.11	0.39	0.23	0.39	0.12
l_{fus} [m]	65.4	65.4	92.3	90.5	65.4	65.4
L/D_{cr} [-]	21.6	20.4	19.7	20.4	21.4	20.3
T/W_{TO} [-]	0.26	0.29	0.25	0.25	0.27	0.29
T_{TO} [kN]	339	392	296	308	347	384
$TSFC_{cr}$ [10^{-5}kg/(N s)]	1.20	1.46	0.430	0.465	1.20	1.45
$\eta_{ov,cr}$ [-]	37%	42%	37%	40%	36%	41%
$N_{AC,\,max}$ [10^3]	1.9	1.4	1.9	1.6	1.9	1.4
t_{bl} [hrs]	10h13m	7h41m	10h13m	8h58m	10h12m	7h49m
SEC_{cr} [10^{-4}MJ/(N s)]	5.18	6.29	5.16	5.58	5.21	6.32
Energy [MJ/(pax km)]	0.70	0.69	0.79	0.73	0.70	0.70

Acknowledgments

This research is sponsored by the European Union's Clean Sky 2 Thematic Topics program (H2020-EU.3.4.5.10.) with grant agreement nr. 865300.

References

[1] Air Transport Action Group (ATAG), "Waypoint 2050," Tech. rep., Sep 2021.

[2] Clean Sky 2 JU and Fuel Cells and Hydrogen 2 JU, "Hydrogen-powered aviation: A fact-based study of hydrogen technology, economics, and climate impact by 2050," Tech. rep., May 2020. https://doi.org/10.2843/471510.

[3] de Jong, S., Antonissen, K., Hoefnagels, R., Lonza, L., Wang, M., Faaij, A., and Junginger, M., "Life-cycle analysis of greenhouse gas emissions from renewable jet fuel production," *Biotechnology for Biofuels*, Vol. 10, No. 64, 2017. https://doi.org/10.1186/s13068-017-0739-7.

[4] World Economic Forum, "Clean Skies for Tomorrow - Sustainable Aviation Fuels as a Pathway to Net-Zero Aviation," Tech. rep., Nov 2020.

[5] Moore, R. H., Thornhill, K. L., Weinzierl, B., Sauer, D., D'Ascoli, E., Kim, J., Lichtenstern, M., Scheibe, M., Beaton, B., Beyersdorf, A. J., Barrick, J., Bulzan, D., Corr, C. A., Crosbie, E., Jurkat, T., Martin, R., Riddick, D., Shook, M., Slover, G., Voigt, C., White, R., Winstead, E., Yasky, R., Ziemba, L. D., Brown, A., Schlager, H., and Anderson, B. E., "Biofuel blending reduces particle emissions from aircraft engines at cruise conditions," *Nature*, Vol. 543, No. 7645, 2017, pp. 411–415. https://doi.org/10.1038/nature21420.

[6] Burkhardt, U., Bock, L., and Bier, A., "Mitigating the contrail cirrus climate impact by reducing aircraft soot number emissions," *npj Climate and Atmospheric Science*, Vol. 1, No. 1, 2018, p. 37. https://doi.org/10.1038/s41612-018-0046-4.

[7] Contreras, A., Yiğit, S., Özay, K., and Veziroğlu, T., "Hydrogen as aviation fuel: a comparison with hydrocarbon fuels," *International Journal of Hydrogen Energy*, Vol. 22, No. 10-11, 1997, pp. 1053–1060.

[8] Ström, L., and Gierens, K., "First simulations of cryoplane contrails," *Journal of Geophysical Research: Atmospheres*, Vol. 107, No. D18, 2002, pp. AAC 2–1–AAC 2–13. https://doi.org/10.1029/2001JD000838.

[9] Marquart, S., Ponater, M., Ström, L., and Gierens, K., "An upgraded estimate of the radiative forcing of cryoplane contrails," *Meteorologische Zeitschrift*, Vol. 14, 2005, pp. 573–582. https://doi.org/10.1127/0941-2948/2005/0057.

[10] Lefebvre, A. H., and Ballal, D. R., *Gas turbine combustion: alternative fuels and emissions*, 3rd ed., CRC press, 2010.

[11] Svensson, F., Hasselrot, A., and Moldanova, J., "Reduced environmental impact by lowered cruise altitude for liquid hydrogen-fuelled aircraft," *Aerospace Science and Technology*, Vol. 8, No. 4, 2004, pp. 307–320. https://doi.org/10.1016/j.ast.2004.02.004.

[12] Gangoli Rao, A., Yin, F., and Werij, H., "Energy Transition in Aviation: The Role of Cryogenic Fuels," *Aerospace*, Vol. 7, 2020, p. 181. https://doi.org/10.3390/aerospace7120181.

[13] Khandelwal, B., Karakurt, A., Sekaran, P. R., Sethi, V., and Singh, R., "Hydrogen powered aircraft : The future of air transport," *Progress in Aerospace Sciences*, Vol. 60, 2013, pp. 45–59. https://doi.org/10.1016/j.paerosci.2012.12.002.

[14] Verstraete, D., Hendrick, P., Pilidis, P., and Ramsden, K., "Hydrogen fuel tanks for subsonic transport aircraft," *International Journal of Hydrogen Energy*, Vol. 35, No. 20, 2010, pp. 11085–11098. https://doi.org/10.1016/j.ijhydene.2010.06.060.

[15] Proesmans, P., and Vos, R., "Hydrogen, Medium-Range Airplane Design Optimization for Minimal Global Warming Impact," *Aerospace Europe Conference 2021*, The Council of European Aerospace Societies (CEAS), Warsaw, 2021.

[16] Proesmans, P., and Vos, R., "Airplane Design Optimization for Minimal Global Warming Impact," *AIAA Scitech 2021 Forum*, American Institute of Aeronautics and Astronautics (AIAA), Virtual event, 2021, p. 1297. https://doi.org/10.2514/6.2021-1297.

[17] Torenbeek, E., *Synthesis of Subsonic Airplane Design*, Delft University Press and Kluwer Academic Publishers, Dordrecht, 1982.

[18] Raymer, D., *Aircraft design: a conceptual approach*, American Institute of Aeronautics and Astronautics, Inc., 2012.

[19] Mattingly, J. D., Heiser, W. H., and Pratt, D. T., *Aircraft Engine Design*, 2nd ed., American Institute of Aeronautics and Astronautics (AIAA), 2002. https://doi.org/10.2514/4.861444.

[20] Schwartz Dallara, E., Kroo, I. M., and Waitz, I. A., "Metric for Comparing Lifetime Average Climate Impact of Aircraft," *AIAA Journal*, Vol. 49, No. 8, 2011, pp. 1600–1613. https://doi.org/10.2514/1.J050763.

[21] Gierens, K., Braun-Unkhoff, M., Le Clercq, P., Plohr, M., Schlager, H., and Wolters, F., "Condensation trails from biofuels/kerosene blends scoping study," Tech. Rep. ENER/C2/2013-627, Deutsches Zentrum für Luft- und Raumfahrt (DLR), 2016.

[22] Wolters, F., Becker, R.-G., and Schaefer, M., "Impact of Alternative Fuels on Engine Performance and CO_2-emissions," *28th International Congress of the Aeronautical Sciences (ICAS), Brisbane, Australia*, Vol. 23, 2012.

[23] Walsh, P. P., and Fletcher, P., *Gas turbine performance*, 2nd ed., Blackwell Science Ltd, Oxford, 2004.

[24] Torenbeek, E., "The initial calculation of range and mission fuel during conceptual design," Tech. Rep. LR-525, Delft University of Technology, Faculty of Aerospace Engineering, 1987.

[25] Dallara, E. S., and Kroo, I., "Aircraft Design for Reduced Climate Impact," *49th AIAA Aerospace Sciences Meeting including the New Horizons Forum and Aerospace Exposition*, American Institute of Aeronautics and Astronautics, Orlando, Florida, 2011. https://doi.org/10.2514/6.2011-265.

[26] Sausen, R., and Schumann, U., "Estimates of the Climate Response to Aircraft CO_2 and NO_x Emissions Scenarios," *Climate Change*, Vol. 44, 2000, pp. 27 – 58. https://doi.org/10.1023/A:1005579306109.

[27] Cherubini, F., Bird, N. D., Cowie, A., Jungmeier, G., Schlamadinger, B., and Woess-Gallasch, S., "Energy- and greenhouse gas-based LCA of biofuel and bioenergy systems: Key issues, ranges and recommendations," *Resources, Conservation and Recycling*, Vol. 53, No. 8, 2009, pp. 434–447. https://doi.org/https://doi.org/10.1016/j.resconrec.2009.03.013.

[28] Moore, R., Thornhill, K., Weinzierl, B., Sauer, D., D'Ascoli, E., Kim, J., Lichtenstern, M., Scheibe, M., Beaton, B., Beyersdorf, A., et al., "Biofuel blending reduces particle emissions from aircraft engines at cruise conditions," *Nature*, Vol. 543, No. 7645, 2017, pp. 411–415. https://doi.org/https://doi.org/10.1038/nature21420.

[29] Unterstrasser, S., "Large-eddy simulation study of contrail microphysics and geometry during the vortex phase and consequences on contrail-to-cirrus transition," *Journal of Geophysical Research: Atmospheres*, Vol. 119, No. 12, 2014, pp. 7537–7555.

[30] Marek, C., Smith, T., and Kundu, K., "Low Emission Hydrogen Combustors for Gas Turbines Using Lean Direct Injection," *41st AIAA/ASME/SAE/ASEE Joint Propulsion Conference & Exhibit*, 2005. https://doi.org/10.2514/6.2005-3776.

[31] Dahl, G., and Suttrop, F., "Engine control and low-NOx combustion for hydrogen fuelled aircraft gas turbines," *International Journal of Hydrogen Energy*, Vol. 23, No. 8, 1998, pp. 695–704. https://doi.org/10.1016/S0360-3199(97)00115-8.

[32] Hydrogen Council, "Path to hydrogen competitiveness: A cost perspective," Tech. rep., Jan 2020.

[33] Roskam, J., *Airplane Design. Part VIII: Airplane Cost Estimation: Design, Development, Manufacturing and Operating*, DARcorporation, 1985.

[34] Embraer S.A, "Embraer 175 Airport Planning Manual," Tech. rep., Embraer S.A, 2021.

[35] Airbus S.A.S. Customer Services, "Airbus A320 Aircraft Characteristics Airport and Maintenance Planning," Tech. rep., Airbus S.A.S. Customer Services, 2019.

[36] Airbus S.A.S. Customer Services, "Airbus A350 Aircraft Characteristics Airport and Maintenance Planning," Tech. rep., Airbus S.A.S. Customer Services, 2020.

[37] Swelbar, W. S., and Belobaba, P. P., "Airline Data Project," , 2019. URL http://web.mit.edu/airlinedata/www/default.html.

[38] Regional Airline Association, "2021 The Year of Community," Tech. rep., Regional Airline Association, 2021.

[39] York, M. A., Hoburg, W. W., and Drela, M., "Turbofan Engine Sizing and Tradeoff Analysis via Signomial Programming," *Journal of Aircraft*, Vol. 55, No. 3, 2018, pp. 988–1003. https://doi.org/10.2514/1.C034463.

[40] Greitzer, E. M., Bonnefoy, P., de la Rosa Blanco, E., Dorbian, C., Drela, M., Hall, D., Hansman, R., Hileman, J., Liebeck, R., Lovegren, J., Mody, P., Pertuze, J., Sato, S., Spakovszky, Z., Tan, C., Hollman, J., Duda, J., Fitzgerald, N., Houghton, J., Kerrebrock, J., Kiwada, G., Kordonowy, D., Parrish, J., Tylko, J., Wen, E., and Lord, W., "N+3 Aircraft Concept Designs and Trade Studies. Volume 2: Appendices - Design Methodologies for Aerodynamics, Structures, Weight, and Thermodynamic Cycles," Tech. Rep. NASA/CR-2010-216794/VOL2, National Aeronautics and Space Administration (NASA), 2010.

[41] IHS Markit, "General Electric CF34," *Jane's Aero-Engines*, IHS Markit, 2021.